Electronic Supplementary Information

Integrative Solar Absorbers for Highly Efficient Solar Steam Generation

Xiaofeng Lin, Jiayao Chen, Zhongke Yuan, Meijia Yang, Guojian Chen, Dingshan Yu, Mingqiu Zhang, Wei Hong,* and Xudong Chen*

Key Laboratory for Polymeric Composite and Functional Materials of Ministry of Education,
Guangdong Engineering Technology Research Center for High-performance Organic and Polymer Photoelectric Functional Films,
School of Chemistry,
Sun Yat-sen University,
Guangzhou 510275, China
E-mail: hongwei9@mail.sysu.edu.cn; cescxd@mail.sysu.edu.cn

Calculation of porosity and density.

The porosity is provided as a fraction of the void volume in the total volume.[S1]

$$\Theta = \frac{V_{void}}{V_{total}} \times 100\% = 1 - \frac{V_{solid}}{V_{total}} \times 100\% \qquad (1)$$

The V_{void} is volume of pores, the V_{solid} is volume of solid and the V_{total} is total volume of foam material including the solid and pore volume. The V_{total} of the cuboid foam can be expressed as V_{total} = a*b*c. The a, b and c represent the three dimensions of the foam, respectively. The V_{solid} can be expressed as V_{solid} = m/ρ_{solid}; the m is the weight of foam and the ρ_{solid} is the solid density of foam materials. The ρ_{solid} of melamine obtained from business is about 1.573 g·cm^{-3}. The ρ_{solid} of the ISA, which is carbonized at low temperature of 400-800 ˚C, is about 1.6-1.8 g·cm^{-3} (between the pure melamine and carbon (ca. 1.8 g·cm^{-3})).[S1]

For example, a piece of unprocessed melamine foam (MF) with volume of 10.0 cm×6.0 cm×2.0 cm (120 cm^3) weights 0.9626 g. Hence, the porosity can be calculated as:

$$1-\frac{0.9626g}{1.573g\cdot cm^{-3}\times 120cm^{-3}}\times 100\% = 99.49\%$$

The total density of the foam materials (ρ_{total}) are calculated as ratio of foam weight (m) to V_{total},

$$\rho_{total} = \frac{m}{V_{total}} \qquad (2)$$

Table S1. Summary of various parameters for the unprocessed MF and integrative solar absorbers (ISAs).

Samples	Mass [g]	V_{total} [cm^{-3}]	ρ_{total} [$mg\cdot cm^{-3}$]	ρ_{solid} [$g\cdot cm^{-3}$]	V_{solid} [cm^{-3}]	Porousity [%]	Thermal conductivity [$W\cdot m^{-1}k^{-1}$]
Unprocessed MF	0.9626	120 (10*6*2)	8.022	1.573	0.612	99.49	0.03669
ISA-400	0.4520	61 (8*4.8*1.6)	7.356	1.6-1.8	0.251-0.282	99.54-99.59	0.03198
ISA-550	0.2518	33 (6.5*3.9*1.3)	7.641	1.6-1.8	0.140-0.157	99.52-99.58	0.02856
ISA-700	0.1233	15 (5*3*1)	8.221	1.6-1.8	0.068-0.077	99.49-99.54	0.03022

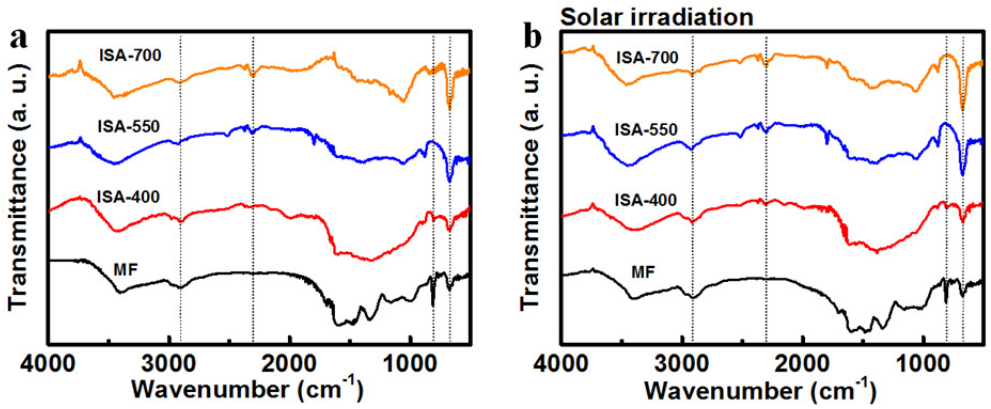

Fig. S1 The FTIR spectra of the unprocessed MF, ISA-400, ISA-550 and ISA-700 a) without and b) with solar irradiation.

Fig. S1 shows the FTIR spectra of the unprocessed MF and the ISAs at different temperatures. The spectrum of the unprocessed MF presents peaks at 880, 1602, 2930 and 3450 cm^{-1} that were assigned to the triazine ring bending, C-N stretching in triazine ring, C-H stretching, and N-H, respectively. The peaks in the range 1300-1500 cm^{-1} can either be attributed to the C-H bending, or to the C-N stretching modes of the s-triazine ring. The peaks in the 1050-1700 cm^{-1} region disappeared when heating above 400 °C to form a very broad band. The intensity of the peak at 880 cm^{-1} (s-triazine bending) gradually faded during the thermal treatment. This disappearance was in relation with the growth of the peaks in the 2230 cm^{-1} range attributed to the C≡N stretching (or C≡C), which indicated the thermal decomposition of the triazine ring. The intensity of the peak 2930 cm^{-1} deceased during the thermal treatment, but still maintained a certain intensity, which indicated the existence of aliphatic carbon (polymeric chain).

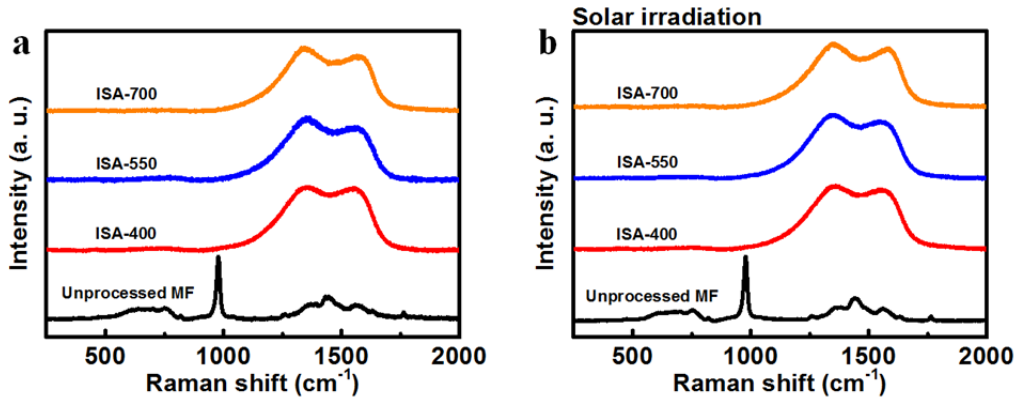

Fig. S2 The Raman spectra of the unprocessed MF, ISA-400, ISA-550 and ISA-700 a) without and b) with solar irradiation.

The Raman spectra (Fig. S2) of the unprocessed MF shows an intense peak at 978 cm^{-1}, characteristic of the breathing modes of the triazine ring of melamine. Two Raman bands are characteristic of melamine: 670 cm^{-1} and 978 cm^{-1}. The first corresponds to the in-plane deformation vibrational mode and the second to the triazine ring breathing vibrational mode. Upon the pyrolysis temperature of 400 °C, the 978 cm^{-1} peak vanished and two new peaks assigned to the carbon D-band (1343-1353 cm^{-1}) and G-band (1550-1580 cm^{-1}) appeared. The D-band corresponds to the disorder-induced due to breathing modes in rings, and, the G-band to the C-C stretching modes in both rings and chains. So, the ISAs were made of a sp^2 carbon network. The decrease of the width of the D-band and G-band were also observed with the increase of the pyrolysis temperature, which constitutes a signature of the carbonization process.

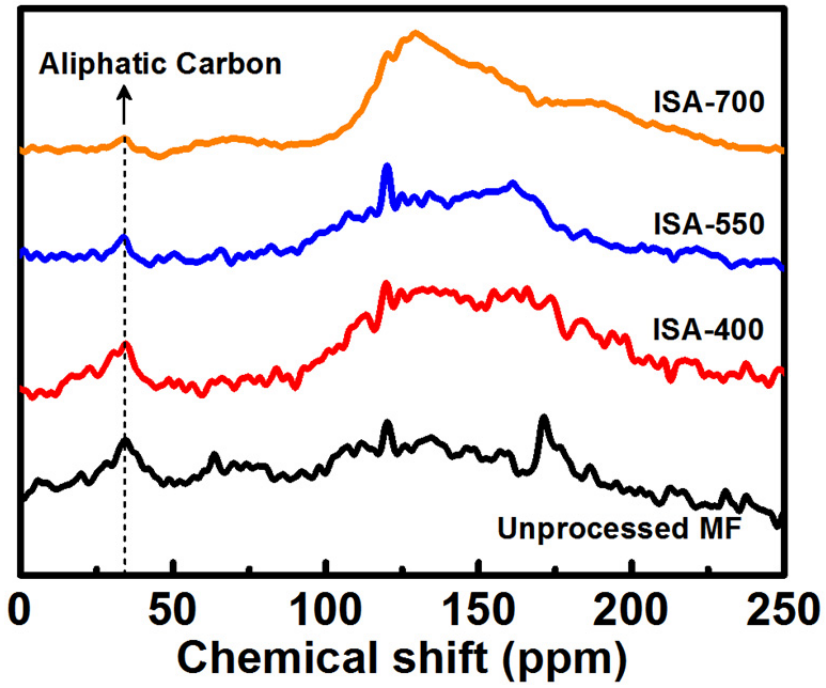

Fig. S3 The ^{13}C solid state CP-MAS NMR spectra of unprocessed MF, ISA-400, ISA-550 and ISA-700. The ^{13}C solid state CP-MAS NMR spectra exhibits the peaks at 34.5 ppm, which assigned to the aliphatic carbon.

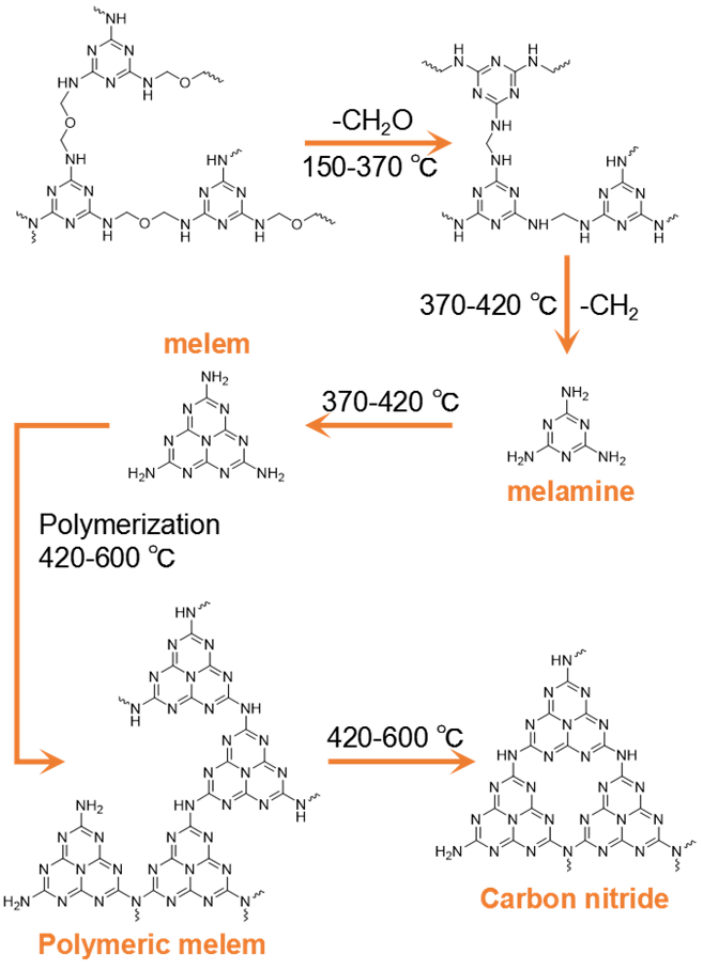

Fig. S4 The possible formation mechanism of the ISA via the calcination process under the nitrogen atmosphere.

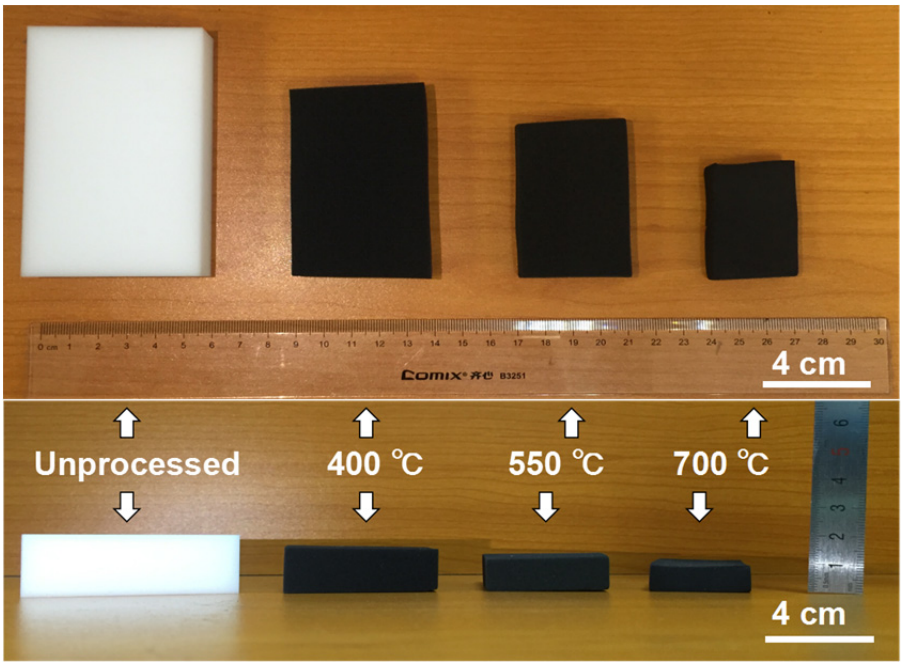

Fig. S5 The photographs of unprocessed MF (10.0 cm×6.0 cm×2.0 cm), ISA-400 (8.0 cm×4.8 cm×1.6 cm), ISA-550 (6.5 cm×3.9 cm×1.3 cm) and ISA-700 (5.0 cm×3.0 cm×1.0 cm).

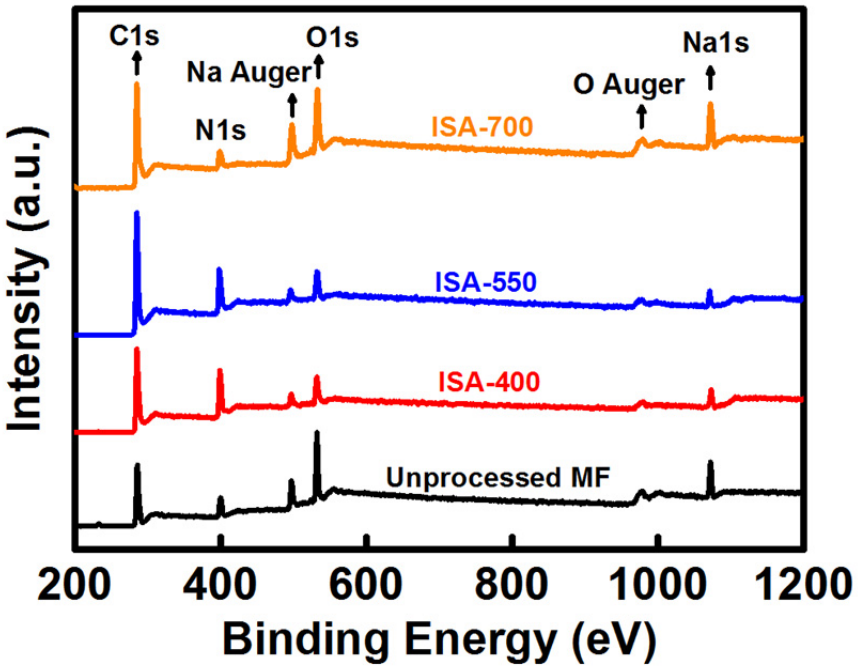

Fig. S6 Full-range XPS spectra of the unprocessed MF, ISA-400, ISA-550 and ISA-700.

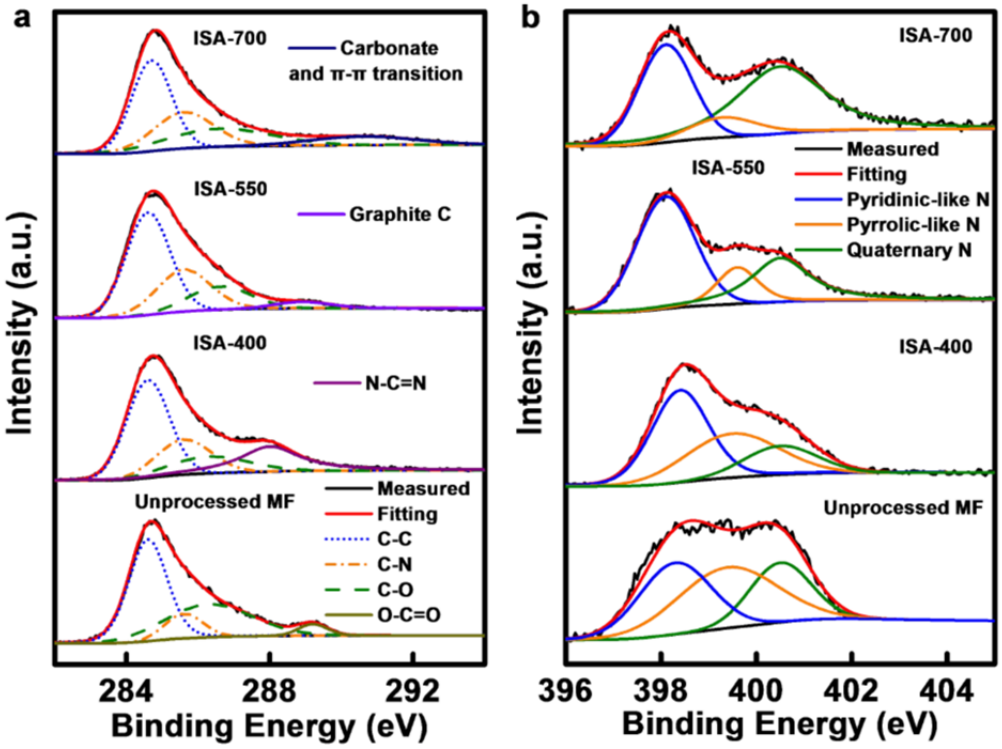

Fig. S7 a) C 1s XPS spectra of the unprocessed MF, ISA-400, ISA-550 and ISA-700. b) N 1s XPS spectra of unprocessed MF, ISA-400, ISA-550 and ISA-700. The C 1s and N 1s spectra were decomposed to several peaks that were fitted by the Gaussian function.

Table S2. The results of elemental analysis for unprocessed MF, ISA-400, ISA-550 and ISA-700.

Samples	C (wt %)	H (wt %)	N (wt %)	C/N ratio
Unprocessed MF	35.27	4.095	43.78	0.806
ISA-400	45.59	2.353	39.03	1.168
ISA-550	49.40	1.694	32.62	1.514
ISA-700	51.61	1.495	24.04	2.147

Table S3. The percentage of pyridinic-like N, pyrrolic-like N and quaternary N nitrogen in nitrogen from XPS for unprocessed MF, ISA-400, ISA-550 and ISA-700.

Samples	Pyridinic-like N (%)	Pyrrolic-like N (%)	Quaternary N (%)
Unprocessed MF	34.75	40.65	24.60
ISA-400	47.67	34.63	17.70
ISA-550	56.08	14.59	29.32
ISA-700	37.72	10.37	51.91

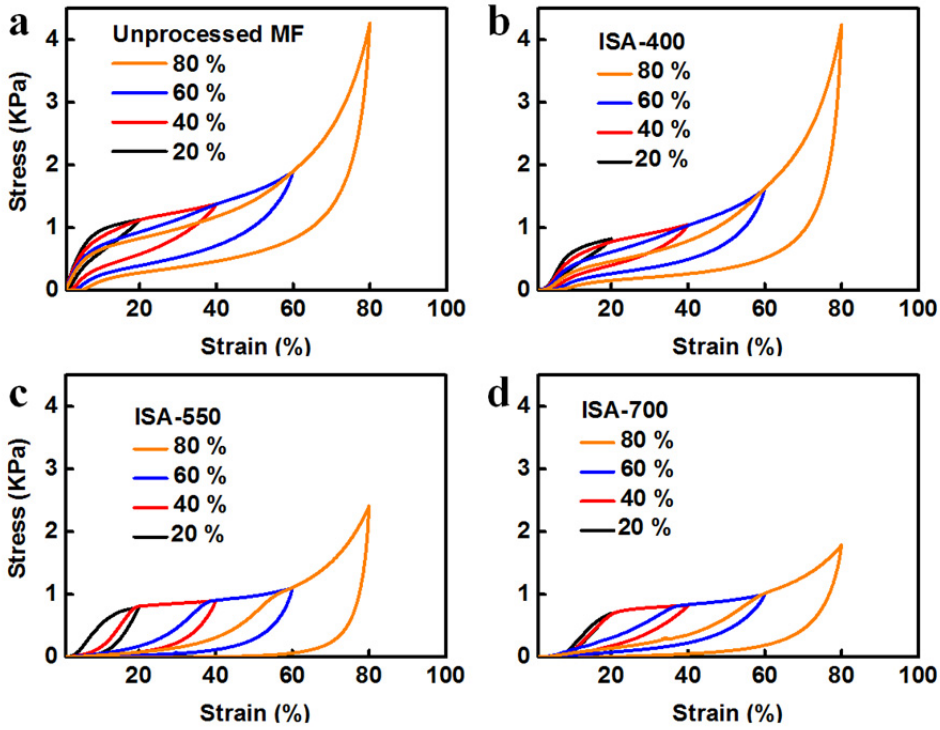

Fig. S8 The stress–strain curves of a) unprocessed MF, b) ISA-400, c) ISA-550 and d) ISA-700 at different strain of 20 %, 40 %, 60 % and 80 %, respectively. For tensile test, the 1 cm thick samples (unprocessed MF or various ISAs) were cut into 3 cm × 3 cm for tensile test, and the strain rate is 20 % per minute.

Table S4. The maxmum stress of unprocessed MF, ISA-400, ISA-550 and ISA-700 at different strain of 20 %, 40 %, 60 % and 80 %, respectively.

Samples Stress (KPa) Strain(%)	20	40	60	80
Unprocessed MF	1.129	1.380	1.898	4.268
ISA-400	0.824	1.049	1.616	4.237
ISA-550	0.795	0.897	1.103	2.410
ISA-700	0.699	0.829	1.003	1.786

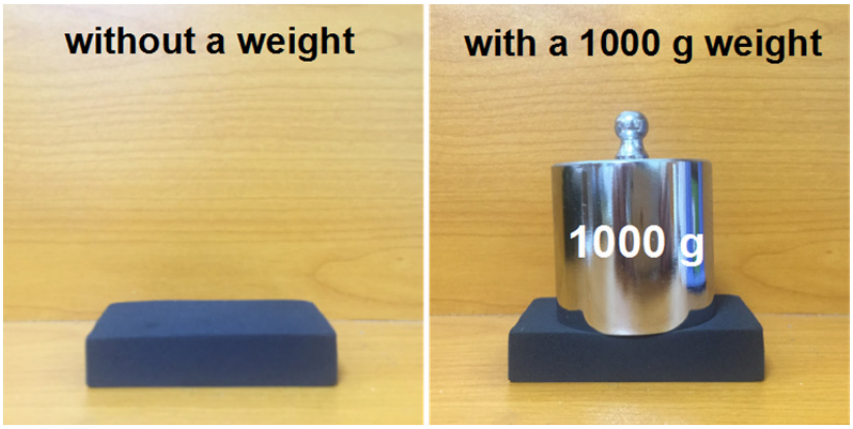

Fig. S9 The photographs of ISA-550 showing its mechanical robustness that can support a 1000 g weight with little compressive deformation.

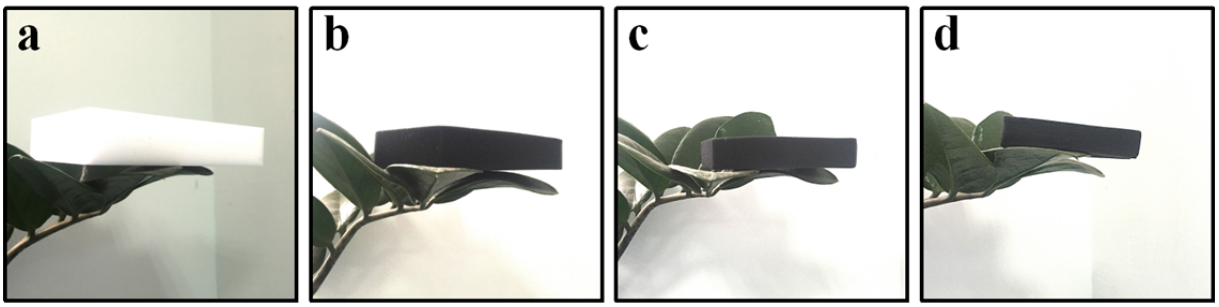

Fig. S10 The photographs of a) unprocessed MF, b) ISA-400, c) ISA-550 and d) ISA-700 showing that they can be lightly put on a cinnamon leaf without any deformation of the leaf.

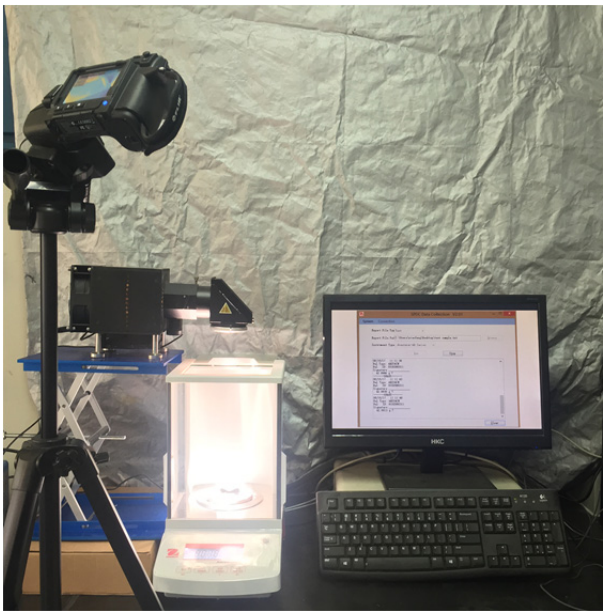

Fig. S11 The photograph of the test system for energy conversion efficiency (η_{ECE}).

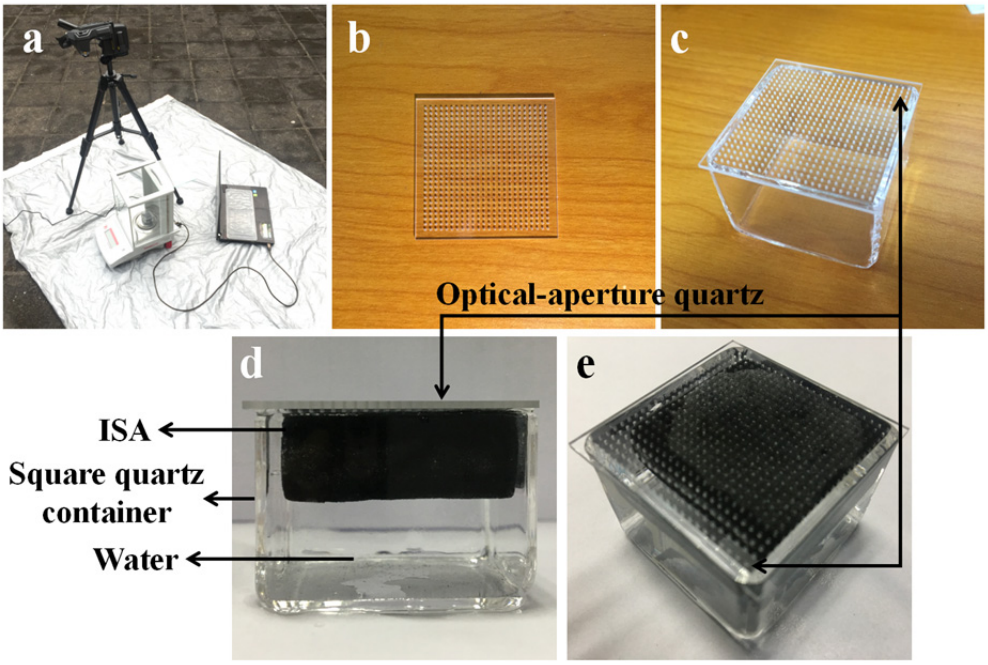

Fig. S12 The photographs of a) the test system under the natural sunlight, b) optical-aperture quartz, c) a square quartz container with a quartz cover, d) and e) the ISA in the square quartz container with a holey quartz cover. The holey quartz cover was used to prevent the impact from the airflow and the light intensity was measured under the quartz cover. In addition, the square quartz container was used to fit the size of ISAs to prevent the redundant bare water.

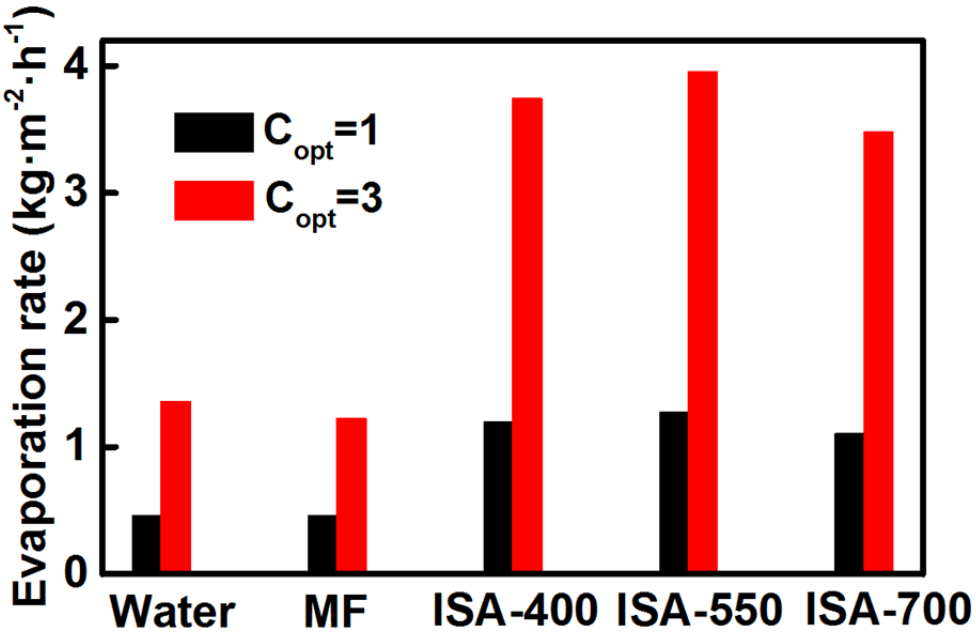

Fig. S13 The bar chart of the water evaporation rates with corresponding samples under 1 sun (black bars) and 3 sun illumination (red bars).

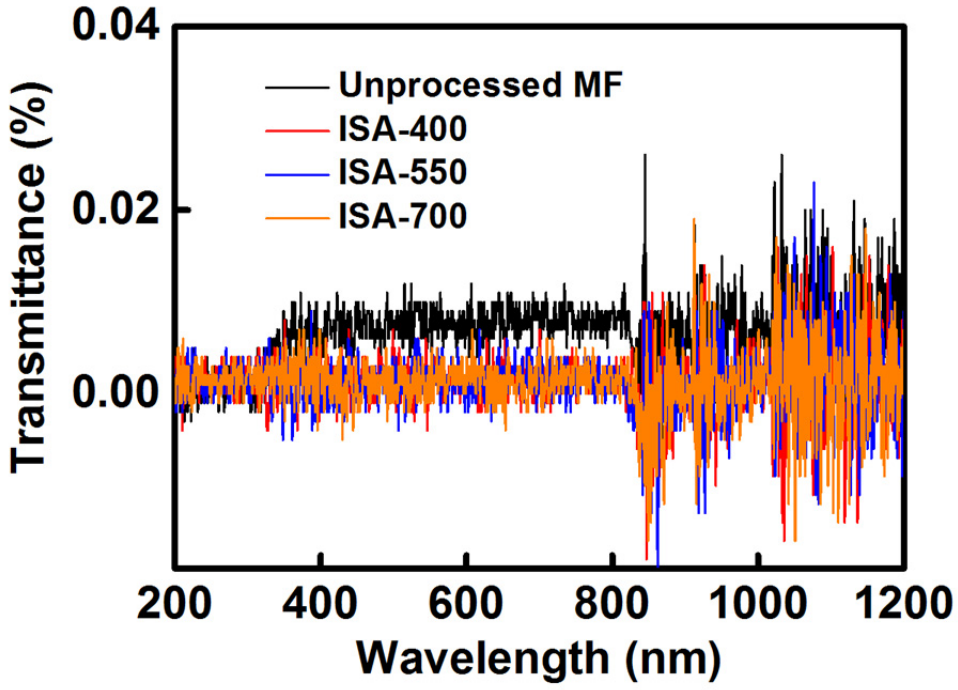

Fig. S14 The transmittance spectra of unprocessed MF, ISA-400, ISA-550 and ISA-700.

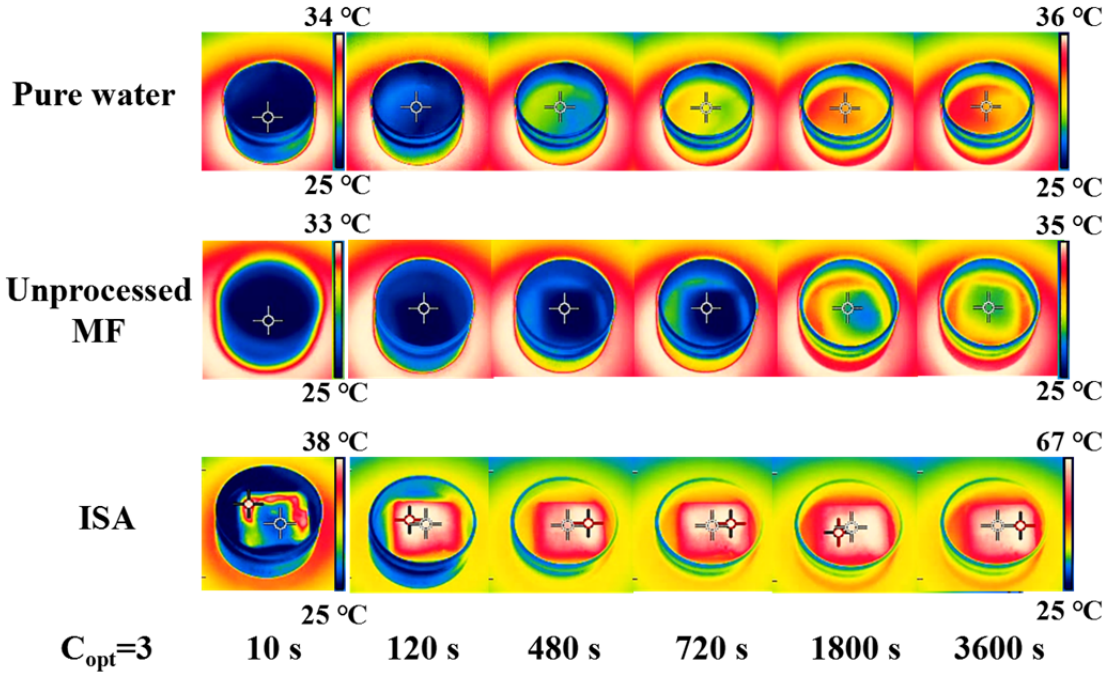

Fig. S15 IR images of the pure water, unprocessed MF and ISA (with water immersion) under solar illumination with a power density of 3 kW·m^{-2}. The images of sequence from left to right are corresponding to t= 10 s, 120 s, 280 s, 720 s, 1800 s and 3600 s, respectively.

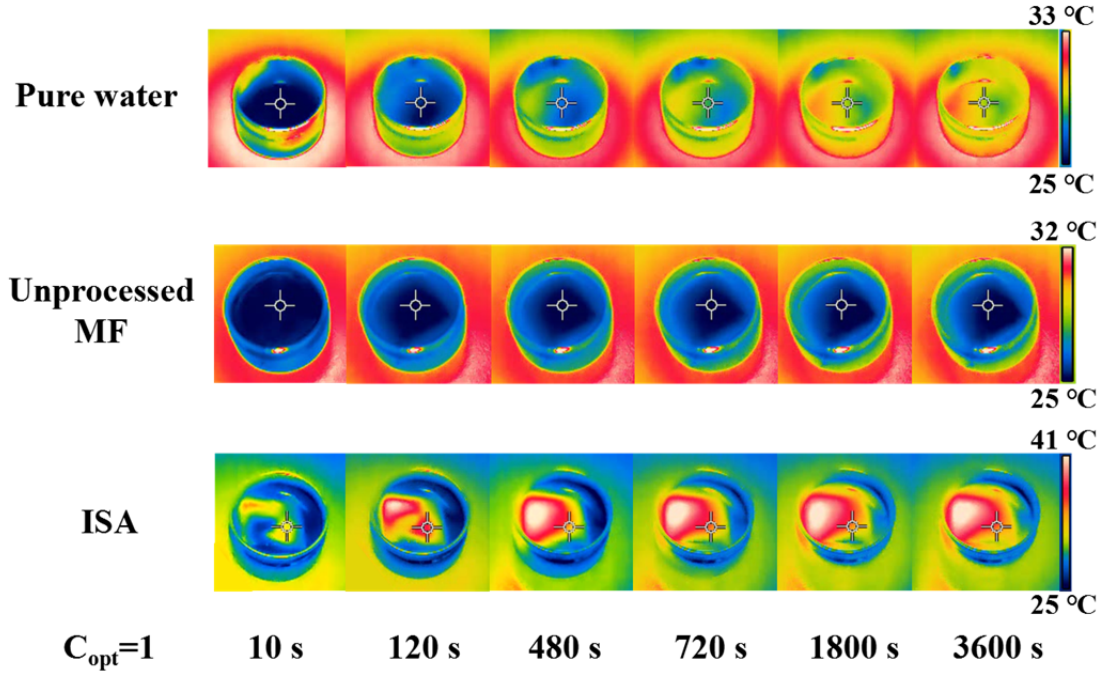

Fig. S16 IR images of the pure water, unprocessed MF and ISA (with water immersion) under solar illumination with a power density of 1 kW·m^{-2}. The images of sequence from left to right are corresponding to t= 10 s, 120 s, 280 s, 720 s, 1800 s and 3600 s, respectively.

Table S5. Calculation results of the energy conversion efficiency (η_{ECE}).

C_{opt}	Evaporation rate of Pure water (kg·m^{-2}·h^{-1})	ṁ (kg·m^{-2}·h^{-1})	Temperature T (℃)	C × (T − T_0) (kJ·kg^{-1})	Δh_{vap} (kJ·kg^{-1})	η_{ECE} (%)[a]	η_{ECE}' (%)[b]
1	0.462	1.270	43.2	76.1	2398.3	87.3	82.3
2	0.996	2.595	58.0	137.9	2362.2	90.1	86.2
3	1.358	3.951	66.6	173.9	2341.1	92.0	88.8
4	1.864	5.332	69.1	184.38	2335.3	93.3	90.3
6	2.877	8.099	72.5	198.6	2327.0	94.7	92.0

a The calculating energy conversion efficiency based on $h_{LV} = C \times (T - T_0) + \Delta h_{vap}$

b The calculating energy conversion efficiency based on h_{LV}=2260 kJ·kg^{-1}

The equation for calculating energy conversion efficiency is $\eta_{ECE} = \dot{m} h_{LV} / C_{opt} P_0$. Among the variable parameters, the total enthalpy of liquid-vapor phase change (h_{LV})

contains two parts, which is the sensible heat and the enthalpy of vaporization (h_{LV}= $C \times (T - T_0) + \Delta h_{vap}$). T_0 is the initial temperature of water (25 ℃). T is the vapor temperature measured by the IR camera (details in Table S5). In the temperature ranging from 40 to 75 ℃, the value of C (specific heat capacity of water) is considered as a constant of 4.18 $J \cdot g^{-1} \cdot K^{-1}$. Meanwhile, Δh_{vap} (the enthalpy of vaporization) is dependent on the temperature, which can be searched from the specialized database.[S2,S3]

Another calculation way of energy conversion efficiency is based on the h_{LV} =2260 $kJ \cdot kg^{-1}$, which was indicated by some former literatures (Adv. Mater. 2015, 27, 4889–4894; ACS Appl. Mater. Interfaces 2016, 8, 9194; ACS Sustain. Chem. Eng. 2016, 4, 1223-1230; ACS Appl. Mater. Interfaces 2016, 8, 31716-31721; J. Mater. Chem. A , 2017, 5, 16212–16219.) For the factor of $\dot{m}$ and P_{in}, it should be noted that the experimental error could occur, including measurement errors of light intensity, the stability of light with long term irradiation, the impact from airflow, ambient temperature and humidity.

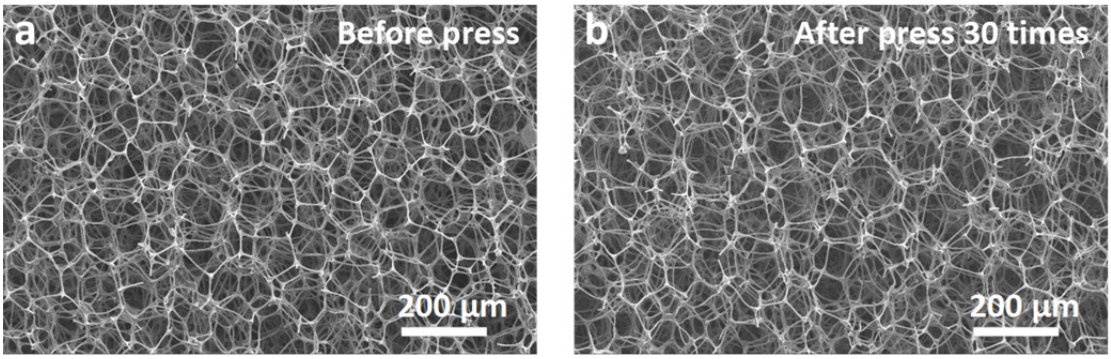

Fig. S17 The SEM images of ISA-550 a) without and b) with pressing 30 times.

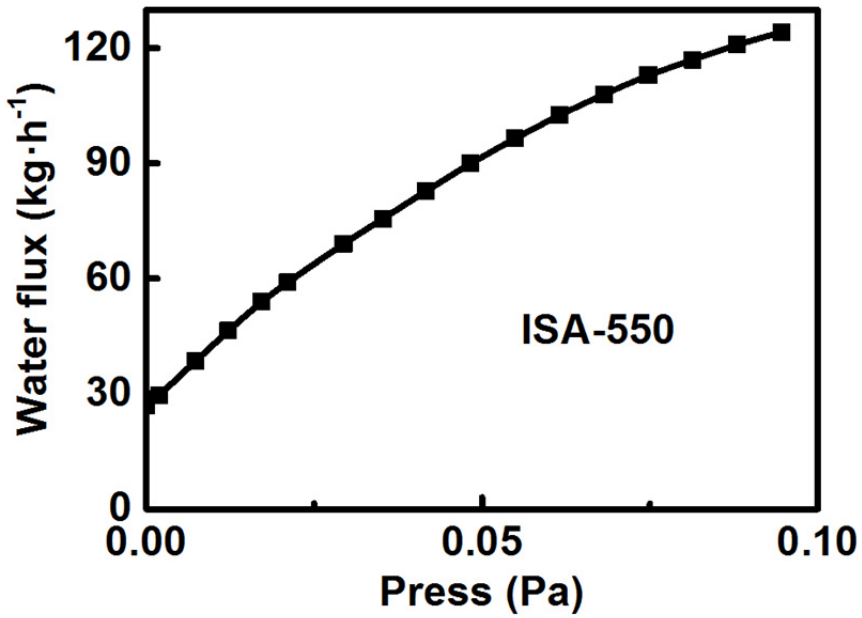

Fig. S18 The water flux–press curves of ISA-550. The intrinsic water flux of ISA-550 has reached up to 27 $kg \cdot h^{-1}$.

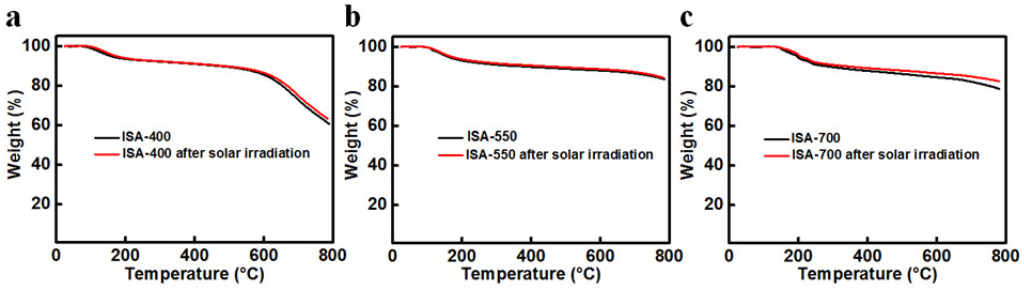

Fig. S19 The TGA curves of the a) ISA-400, b) ISA-550 and c) ISA-700 without and with solar irradiation, under N_2 with a ramp of 5 ℃·min^{-1} from 30 to 800 ℃.

Fig. S20 The photograph of the homemade device for desalination under the natural sunlight.

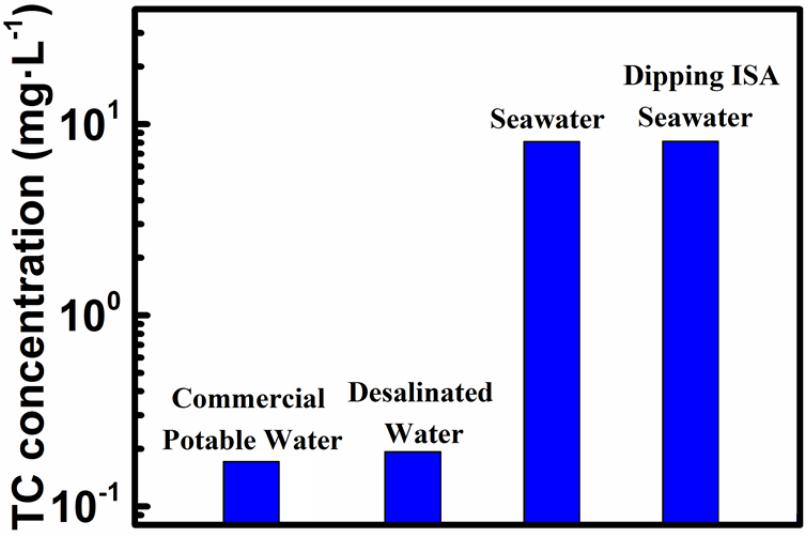

Fig. S21 The total carbon concentration in commercial potable water, desalinated water, seawater and seawater with ISAs dipping in during solar irradiation .

As shown in the figure above, the seawater with ISAs dipping in during solar irradiation exhibits similar total carbon concentration with the original seawater. The desalinated water we obtained has total carbon concentration comparable with the commercial potable water (Cestbon, purified drinking water).

Table S6. The concentrations of Na^+, K^+, Ca^{2+} and Mg^{2+} of the seawater and the desalinated water measured by ICP-AES.

Ions	Na^+ [mg·L^{-1}]	K^+ [mg·L^{-1}]	Ca^{2+} [mg·L^{-1}]	Mg^{2+} [mg·L^{-1}]	Cl^- [mg·L^{-1}]	SO_4^{2-} [mg·L^{-1}]
Seawater	10588	393	482	1132	19670	2610
Desalinated water	2.78	Lower than the detection limit	0.86	0.07	0.04	0.05

Table S7. Summary of recent reports about the water evaporation rate under different solar illumination and thermal condutivities of various solar abosrbers.

Author (year)	Material of solar absorber	Water evaporation rate under corresponding solar illumination (kg·m^{-2}·h^{-1})			Therm-al condu-ctivity (W·m^{-1} K^{-1})	Room temperarture (°C)	Humidity (%)
		1 kW·m^{-2}	2 kW·m^{-2}	3/3.5 kW·m^{-2}			
H. Ghasemi (2014) [S4]	Carbon foam supporting graphite	1.0	2.0	3.0	0.117-0.309	24	31
Y. ITO (2015) [S5]	Multifunctional Porous Graphene	1.5	-	-	9	24	14
J. Lou (2016) [S6]	Paper-Based rGO Composites	-	-	2.8	0.05	-	.-
X. Wang (2016) [S7]	rGO-supported Fe_3O_4 magnetic nanoparticles	1.12	2.25	-	-	32	30

L. Zhou (2016) [S8]	Aluminium-based plasmonic structure	1.0	2.3	3.8	-	24	48
L. Zhou (2016) [S9]	Plasmonic absorbers	1.2	2.2	3.7	-	24	42
X. Hu (2017) [S10]	Graphene oxide-based aerogels	1.622	-	-	0.05	25	45
Z. Liu (2017) [S3]	Polystyrene foam supporting carbon-coated paper	1.28	-	3.66	0.04	21	10
X. Wang (2017) [S11]	Plasmonic membranes	0.87	2.2	3.5	-	18	-
C. Chen (2017) [S12]	Carbon nanotube -modified flexible wood membrane	0.95	-	2.88	0.21	-	-
This Work	**ISAs**	**1.270**	**2.595**	**3.951**	**0.028**	**25**	**50**

Table S8. Summary of recent reports about the energy conversion efficiency under different solar illumination of various solar abosrbers.

Author (year)	**Material of solar absorber**	**Energy conversion efficiency under corresponding solar illumination (%)**			**Room temperarture (℃)**	**Humidity (%)**
		1 kW·m^{-2}	**2 kW·m^{-2}**	**3/3.5 kW·m^{-2}**		
H. Ghasemi (2014) [S4]	Carbon foam supporting graphite	64	63	65	24	31
Y. ITO (2015) [S5]	Multifunctional Porous Graphene	80	-	-	24	14
X. Wang (2016) [S7]	rGO-supported Fe_3O_4 magnetic nanoparticles	68	70	-	32	30
L. Zhou (2016) [S8]	Aluminium-based plasmonic structure	57	71	78	24	48

L. Zhou (2016) [S19]	Plasmonic absorbers	63	73	80	24	42
X. Hu (2017) [S10]	Graphene oxide-based aerogels	83	-	-	25	45
Z. Liu (2017) [S3]	Polystyrene foam supporting carbon-coated paper	88.6	-	85.5	21	10
X. Wang (2017) [S11]	Plasmonic membranes	62.5	61	62	18	-
C. Chen (2017) [S12]	Carbon nanotube -modified flexible wood membrane	65	-	67	-	-
This Work	**ISAs**	**87.3**	**90.1**	**92**	**25**	**50**

S1 S. Chen, G. He, H. Hu, S. Jin, Y. Zhou, Y. He, S. He, F. Zhao, H. Hou, *Energy Environ. Sci.* 2013, **6**, 2435.

S2 Dortmund Data Bank Software & Separation Technology, DDBST GmbH, Oldenburg 2016.

S3 Z. Liu, H. Song, D. Ji, C. Li, A. Cheney, Y. Liu, N. Zhang, X. Zeng, B. Chen, J. Gao, Y. Li, X. Liu, D. Aga, S. Jiang, Z. Yu, Q. Gan, *Global Challenge* 2017, **1**, 1600003.

S4 H. Ghasemi, G. Ni, A. M. Marconnet, J. Loomis, S. Yerci, N. Miljkovic, G. Chen, *Nat. Commun*. 2014, **5**, 4449.

S5 Y. Ito, Y. Tanabe, J. H. Han, T. Fujita, K. Tanigaki, M. Chen, *Adv. Mater.* 2015, **27**, 4302.

S6 J. Lou, Y. Liu, Z. Wang, D. Zhao, C. Song, J. Wu, N. Dasgupta, W. Zhang, D. Zhang, P. Tao, W. Shang, T. Deng, *ACS Appl. Mater. Interfaces* 2016, **8**, 14628.

S7 X. Wang, G. Ou, N. Wang, H. Wu, *ACS Appl. Mater. Interfaces* 2016, **8**, 9194.

S8 L. Zhou, Y. Tan, J. Wang, W. Xu, Y. Yuan, W. Cai, S. Zhu, J. Zhu, *Nat. Photonics* 2016, **10**, 393.

S9 L. Zhou, Y. Tan, D. Ji, B. Zhu, P. Zhang, J. Xu, Q. Gan, Z. Yu, J. Zhu, *Sci. Adv.* 2016, **2**, e1501227.

S10 X. Hu, W. Xu, L. Zhou, Y. Tan, Y. Wang, S. Zhu, J. Zhu, *Adv. Mater.* 2017, **29**, 1604031.

S11 X. Wang, Y. He, X. Liu, G. Cheng, J. Zhu, *Applied Energy* 2017, **195**, 414.

S12 C. Chen, Y. Li, J. Song, Z. Yang, Y. Kuang, E. Hitz, C. Jia, A. Gong, F. Jiang, J. Y. Zhu, B.Yang, J. Xie, L. Hu, *Adv. Mater.* 2017, 1701756.